Hyperfine and Spin-Orbit Coupling Effects on Decay of Spin-Valley States in a Carbon Nanotube

T. Pei,[1,*] A. Pályi,[2] M. Mergenthaler,[1] N. Ares,[1] A. Mavalankar,[1] J. H. Warner,[1] G. A. D. Briggs,[1] and E. A. Laird[1,†]
[1]Department of Materials, University of Oxford, Parks Road, Oxford OX1 3PH, United Kingdom
[2]Department of Physics and MTA-BME Condensed Matter Research Group, Budapest University of Technology and Economics, 1111 Budapest, Hungary
(Received 7 July 2016; published 25 April 2017)

The decay of spin-valley states is studied in a suspended carbon nanotube double quantum dot via the leakage current in Pauli blockade and via dephasing and decoherence of a qubit. From the magnetic field dependence of the leakage current, hyperfine and spin-orbit contributions to relaxation from blocked to unblocked states are identified and explained quantitatively by means of a simple model. The observed qubit dephasing rate is consistent with the hyperfine coupling strength extracted from this model and inconsistent with dephasing from charge noise. However, the qubit coherence time, although longer than previously achieved, is probably still limited by charge noise in the device.

DOI: 10.1103/PhysRevLett.118.177701

The coexistence in carbon nanotubes of spin and valley angular momenta opens a host of possibilities for quantum information [1–4], coherent coupling to mechanics [5,6], and on-chip entanglement [7,8]. Spin-orbit coupling [9] provides electrical control but introduces a relaxation channel. Furthermore, measurements of dephasing and decoherence [10–12] show that spin and valley qubit states couple surprisingly strongly to lattice nuclear spins and to uncontrolled electric fields, e.g., from thermal switchers. Realizing these possibilities requires such effects to be mitigated. Here, we study the leakage current in a Pauli-blockaded double quantum dot to identify spin-orbit and hyperfine contributions to spin-valley relaxation [3,13,14]. By suspending the nanotube, we decouple it from the substrate [11]. Measuring a spin-valley qubit defined in the double dot, we find dephasing and decoherence rates nearly independent of temperature and show that charge noise cannot explain the observed dephasing, supporting the conclusion that despite the low density of ^{13}C spins, hyperfine interaction causes rapid dephasing in nanotubes [10,11].

The measured device [Figs. 1(a)–1(b)] is a carbon nanotube suspended by stamping between two contacts and over five gate electrodes $G1-G5$ [3,15–17]. Gate voltages $V_{G1}-V_{G5}$, together with Schottky barriers at the contacts, define a double quantum dot potential. The dot potentials are predominantly controlled by gates $G1$ (for the left dot) and $G4-G5$ (for the right dot), while the interdot tunnel barrier is controlled by gates $G2-G3$. For fast manipulation, gates $G1$ and $G5$ are connected via tees to waveform generator outputs and a vector microwave source. The device is measured in a magnetic field $\mathbf{B}=(B_X,B_Y,B_Z)$, with Z chosen along the nanotube and X normal to the substrate. Experiments were in a dilution refrigerator at 15 mK unless stated otherwise.

To map charge configurations of the double quantum dot, we measure the current I through the nanotube with source-drain bias $V_{SD}=8$ mV, applied between the contacts [Fig. 1(c)]. As a function of V_{G1} and V_{G4}, the honeycomb Coulomb peak pattern is characteristic of a double quantum dot, with honeycomb vertices marking transitions between particular electron or hole occupations [20]. A horizontal stripe of suppressed current around $V_{G4}=200$ mV indicates depletion of the right dot in this gate voltage range. The width of this stripe implies a band gap of 120 meV. No such suppression is observed as a function of V_{G1}, indicating that the left dot is doped across the entire range. Since at room temperature, conductance decreases with increasing V_{G1}, we believe that the left dot is doped with holes, implying that p-p and p-n double-dot configurations are accessible [21]. Within each honeycomb region, we can therefore assign absolute electron or hole occupations to the right dot but only relative hole occupations to the left dot.

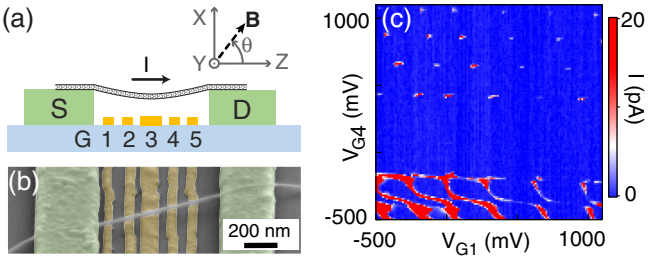

FIG. 1. (a) Schematic and (b) scanning electron microscopy image of a device lithographically identical to the one measured. The nanotube is suspended between contact electrodes (130 nm Cr/Au, marked S and D) and over gate electrodes (20 nm Cr/Au, marked $G1-G5$) patterned on a Si/SiO_2 substrate. Field axes are indicated. For imaging, 2 nm of Pt was evaporated over this chip. (c) Current as a function of gate voltages V_{G1} and V_{G4}, mapping out a double quantum dot stability diagram.

Because tunneling between quantum dots is governed by selection rules on spin and valley quantum numbers, transport through the device is subject to Pauli blockade [22]. This arises because the exclusion principle imposes an energy cost to populate spin-valley triplet states in a single quantum dot. Interdot tunneling from a spin-valley triplet formed between the two dots is therefore blocked, suppressing I for certain gate and bias settings. In this blocked regime, a leakage current gives information about spin and valley relaxation.

We focus on Pauli-blockaded transport with the double dot tuned to a p-n configuration [3,10]. Figure 2(a) shows I as a function of gate voltage near a $(n_h, 1_e) \rightarrow ((n+1)_h, 2_e)$ transition. Here, (n_h,m_e) denotes a configuration with $n_h(m_e)$ holes (electrons) in the left (right) dot. Two overlapping current triangles are seen, as expected for a double-dot Coulomb blockade [20]; in the lower triangle, transport occurs via the cycle of tunneling events $((n+1)_h,1_e)\rightarrow(n_h,1_e)\rightarrow((n+1)_h,2_e)\rightarrow((n+1)_h,1_e)$ and in the upper triangle via $(n_h,2_e)\rightarrow(n_h,1_e)\rightarrow((n+1)_h,2_e)\rightarrow(n_h,2_e)$. The low current near the triangle baselines is indicative of the Pauli blockade suppressing the second step in each sequence, as expected for odd n_h.

To characterize the energy levels and spin-valley relaxation, we measure I as a function of the magnetic field and double-dot detuning ε, defined as the difference of electrochemical potential between left and right dots [3]. Detuning is swept by adjusting V_{G1} and V_{G4} along the diagonal axis marked in Fig. 2(a), with the triangle baselines marking $\varepsilon = 0$. Figure 2 shows data as a function of the magnetic field parallel [Fig. 2(b)] and perpendicular [Fig. 2(c)] to the nanotube and as a function of field angle θ in the XZ plane [Fig. 2(d)]. The triangle edge locations in the gate voltage space give information about the double-dot energy levels; the upper edges in Figs. 2(b)–2(d) correspond to ground-state degeneracy ($\varepsilon = 0$) between left and right dots, while the lower edge marks the degeneracy of the right dot ground state with the Fermi level in the right lead. From the evolution of the lower edge, which maps the energy of the two-electron state, we extract orbital g factor $g_{\mathrm{orb}} \approx 15$, spin-orbit coupling $\Delta_{\mathrm{SO}} \approx 300\ \mu$eV, and valley-mixing parameter $|\Delta_{KK'}| \lesssim 80\ \mu$eV for the right dot, consistent with measurements on neighboring transitions [17] and on other single-wall nanotube devices [9,12,23,24]. However, in similar measurements cutting through the left triangle edge, and therefore tracking levels of the left dot, no clear field dependence was seen [17]. This is explained either by stronger valley mixing $\Delta_{KK'}$ in the left dot (e.g., due to disorder) or by suppression of the valley magnetic moment by large-hole occupation [12,25]. Thus, the single-dot spectrum differs between left and right dots.

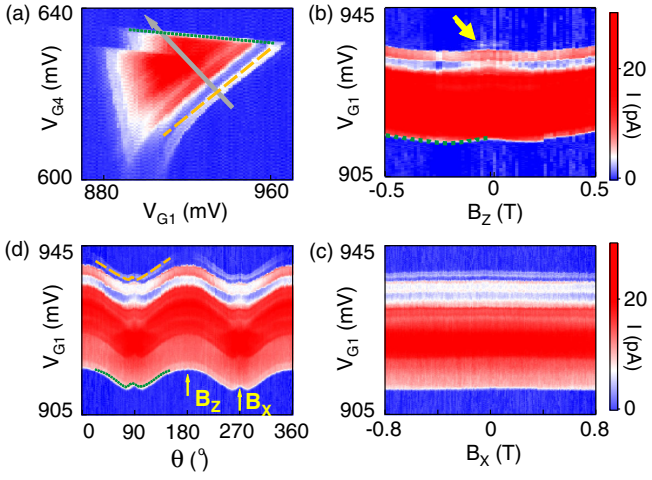

FIG. 2. (a) Current at a Pauli-blocked transition, with $V_{\mathrm{SD}} = 8$ mV, $V_{G2} = V_{G3} = -210$ mV, $\mathbf{B} = 0$. Dashed (dotted) line marks ground-state degeneracy between left and right dots (between right dot and lead). Arrow marks detuning axis. (b) Current as a function of V_{G1} along the detuning axis and of the magnetic field parallel to the nanotube. Arrow marks a region of the Pauli blockade leakage current near zero field. (c) As (b) for perpendicular field. (d) As a function of the field angle for $|\mathbf{B}| = 0.8$ T . Color scales in (a),(d) match (c). Dashed and dotted curves highlight the same transitions as in (a).

We now study the field dependence of the Pauli blockade leakage current to gain insight into spin-valley relaxation mechanisms [3,10,13]. This leakage current is evident for small ε (top of the current band) in Figs. 2(b)–2(d) and shows a strong dependence on field direction. As a function of the magnetic field, the current is maximal around $B_Z = 0$ [Fig. 2(b)] but varies only weakly with B_X [Fig. 2(c)]. In fact, the leakage current can even show a dip at $B_X = 0$ [17]. This different behavior is attributed to different complex phases of $\Delta_{KK'}$ in the two dots, which in a perpendicular field, lead to nonaligned effective Zeeman axes nearly independent of field strength [26,27] and therefore, leads to the leakage current being nearly independent of B_X [17]. Similar behavior in some other systems [28–31] is due to anisotropy of the g factor.

The low-B_Z current peak is an indication of hyperfine-mediated relaxation. To study it in more detail, Fig. 3(a) shows measurements for different settings of the interdot tunnel barrier. Here, the barrier is tuned by the voltage $V_b \equiv V_{G2} = V_{G3}$. For a range of barrier settings, the central peak is accompanied by two side peaks. This contrasts with previous measurements in GaAs, InAs, and InSb, where a hyperfine-induced peak in the Pauli blockade leakage current at zero field evolves to a double peak as tunnel coupling is increased [13,14,31,32]. Here, side peaks instead occur in conjunction with a zero-field peak.

This behavior is explained by considering the effects of hyperfine interaction together with spin-orbit coupling. Consider the zero-field behavior first, and for concreteness, focus on large detuning as shown in Fig. 3(b). The spin-valley degree of freedom, associated with the unpaired particle in each dot, forms an effective spin-$\frac{1}{2}$ Kramers doublet $\{|\Uparrow\rangle, |\Downarrow\rangle\}$. Without hyperfine coupling and

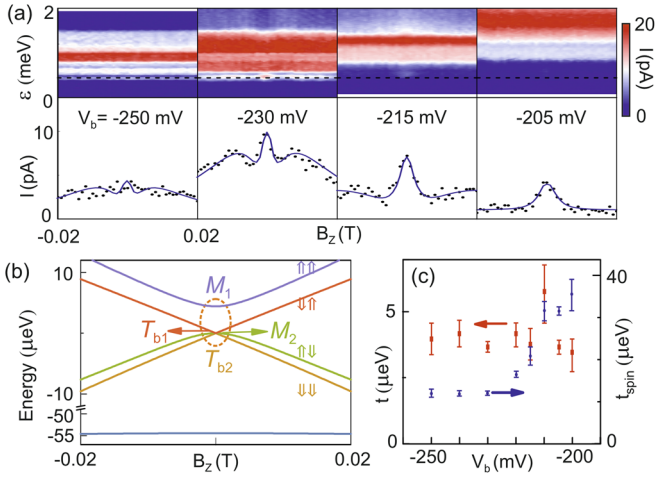

FIG. 3. (a) Field-dependent transition measured with different tunnel barrier gate settings. Upper plots: current as a function of ε and B_Z in the Pauli blockade. Lower plots: cuts along dashed lines of constant detuning. Data (dots) are fitted by a model (curves) described in the text. (b) Schematic energy levels in the absence of hyperfine interaction. The zero-field current peak in (a) is associated with the level degeneracy at $B_Z = 0$ (highlighted by ellipse), where hyperfine interaction mixes blocked and unblocked states. Side peaks are associated with spin-dependent tunneling. (c) Tunnel coupling t and t_{spin} extracted from fits as in (a). Error bars represent 95% confidence intervals.

spin-dependent tunneling, the two-particle states are an effective $((n+1)_h, 2_e)$ singlet ground state $|S_g\rangle$, a singlet excited state $|S\rangle \equiv (1/\sqrt{2})(|\Uparrow\Downarrow\rangle - |\Downarrow\Uparrow\rangle)$, and $(n_h, 1_e)$ triplet states $|T_+\rangle \equiv |\Uparrow\Uparrow\rangle$, $|T_0\rangle \equiv (1/\sqrt{2})(|\Uparrow\Downarrow\rangle + |\Downarrow\Uparrow\rangle)$, and $|T_-\rangle \equiv |\Downarrow\Downarrow\rangle$. In this effective spin basis, the main effect of introducing spin-orbit interaction is to cause spin-dependent tunneling [19,33,34], described by Hamiltonian $H_{\mathrm{tun}} = t|S\rangle\langle S_g| + it_{\mathrm{spin}}|T_u\rangle\langle S_g| + \mathrm{H.c.}$, where t and t_{spin} are, respectively, the spin-conserving and spin-flip tunnel couplings. This Hamiltonian couples one superposition $|T_u\rangle$ of triplet states to the $((n+1)_h, 2_e)$ singlet $|S_g\rangle$, while two orthogonal triplet superpositions $|T_{b1}\rangle$ and $|T_{b2}\rangle$ remain uncoupled. The energy eigenstates of the $(n_h, 1_e)$ configuration are therefore, $|T_{b1}\rangle$, $|T_{b2}\rangle$, $|M_1\rangle$ and $|M_2\rangle$, where $|M_{1,2}\rangle$ are mixtures of $|S\rangle$ and $|T_u\rangle$, and $|M_2\rangle$ remains degenerate with $|T_{b1}\rangle$ and $|T_{b2}\rangle$. Since $|M_1\rangle$ and $|M_2\rangle$ both have a finite $|S\rangle$ component, spin-independent inelastic interdot tunneling processes (e.g., phonon-assisted tunneling) allow charge relaxation into $((n+1)_h, 2_e)$; however, the two uncoupled triplets $|T_{b1}\rangle$ and $|T_{b2}\rangle$ cannot relax in this way and therefore, block the current. The spectrum, including magnetic field dependence, is shown in Fig. 3(b). We now include hyperfine interaction, which acts on both spin and valley degrees of freedom [35,36]. At $\mathbf{B} = 0$, the three energetically aligned states $|T_{b1}\rangle$, $|T_{b2}\rangle$, and $|M_2\rangle$ mix to form new eigenstates $|M_2'\rangle$, $|M_3'\rangle$, $|M_4'\rangle$, each overlapping with $|S\rangle$, therefore contributing to the current via spin-independent inelastic interdot tunneling. In this picture, the triple-peak structure is explained as follows. Each current peak indicates a field strength where the $(n_h, 1_e)$ eigenstates are singlet-triplet mixtures, allowing relaxation to $((n+1)_h, 2_e)$. The central peak arises from hyperfine mixing of three degenerate states [highlighted in Fig. 3(b)]. Side peaks are induced by the interplay of the Zeeman effect and effective spin-dependent interdot tunneling. At large detuning ($\varepsilon \gg t, t_{\mathrm{spin}}$), the energy scale characterizing spin mixing within the $(n_h, 1_e)$ configuration is $t_{\mathrm{spin}}t/\varepsilon$ [17]. In general, the preferred axis for spin-dependent tunneling aligns neither with the nanotube nor with $\mathbf{B}$. In the field range where $t_{\mathrm{spin}}t/\varepsilon \sim \mu_B B_Z$, the $(n_h, 1_e)$ eigenstates are therefore, singlet-triplet mixtures, which results in side peaks in $I(B_Z)$. As B_Z is further increased (such that $\mu_B B_Z \gg t_{\mathrm{spin}}t/\varepsilon$), Zeeman energy dominates spin-orbit-induced mixing so that the eigenstates are $|\Uparrow\Downarrow\rangle$, $|\Downarrow\Uparrow\rangle$, $|T_+\rangle$, and $|T_-\rangle$, where the latter two reestablish the Pauli blockade.

We validate this picture quantitatively by fitting measured current [cuts in Fig. 3(a)], using a model of charge relaxation among the five spin-orbit and hyperfine mixed spin-valley states. Inelastic charge relaxation with rate Γ_{in} causes $(n_h, 1_e)$ states to decay to $((n+1)_h, 2_e)$, based on their overlap with $|S\rangle$. Nuclear-spin fluctuations are incorporated by averaging I over an ensemble of hyperfine configurations [17] with root-mean-square coupling strength E_N. We first fit the second panel using fit parameters Γ_{in}, t, t_{spin}, and E_N. Holding the fitted value $E_N = 0.16 \pm 0.03$ μeV, we then fit across the range of V_b settings. Fitted values of t and t_{spin} are shown in Fig. 3(c). Extracted t is fairly constant over the range, whereas t_{spin} increases with V_b. This presumably reflects that whereas the interdot barrier of an n-p double dot is set by the slope of the potential and not strongly affected by V_b, the Rashba spin-orbit coupling is set by the perpendicular electric field. Unexpectedly, we find $t_{\mathrm{spin}} > t$.

To further explore hyperfine interaction, we characterize a spin-valley qubit at this transition [11]. The qubit is controlled using electrically driven spin resonance (EDSR), with a cycle of gate voltage pulses applied to $G1$ and $G5$ [Fig. 4(a)] [37–39]. The cycle first initializes an effective triplet state by configuring the double dot in the Pauli blockade. The detuning is then pulsed to configure the device in the Coulomb blockade, and a microwave burst at frequency f is applied to $G1$ to manipulate the spin-valley state. Finally, the device is returned to the Pauli blockade; if an effective spin flip has occurred, the Pauli blockade is temporarily lifted, allowing the result of the manipulation to be read out via the current. Repeating the cycle with period ~800 ns, the resulting current change ΔI is detected by chopping the microwaves at 117 Hz and locking in to the chopper signal [38]. The EDSR spectrum [Fig. 4(b)] shows a diagonal line of increased ΔI, indicating resonance when f matches the qubit frequency f_R. The slope gives an

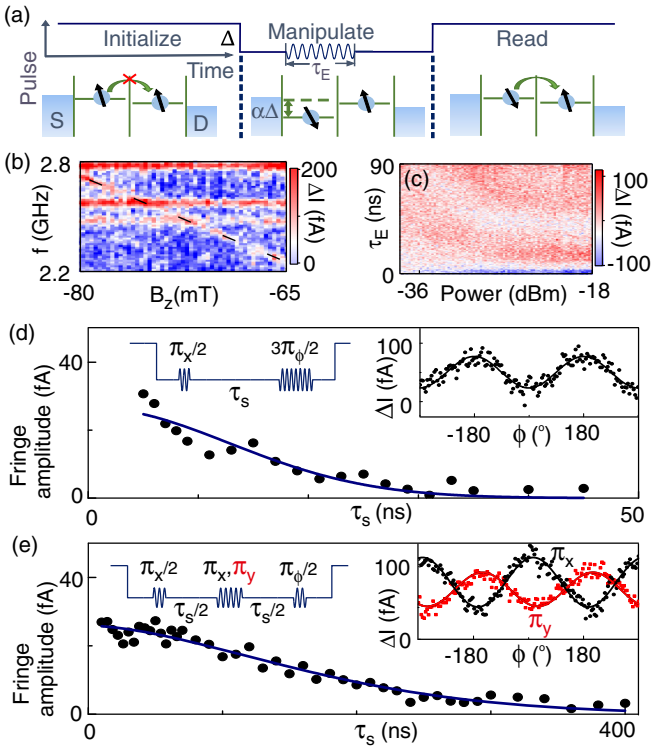

FIG. 4. (a) Pulse scheme for qubit manipulation. Upper panel: gate voltage cycle applied to $G1$. Lower panel: double-dot energy levels during each step. (b) Resonance signal (marked by dashed line) as a function of f and B_Z, with $\theta = 0$, $\tau_E = 40$ ns, and microwave level ~ -20 dBm at the device. (c) Resonant signal as a function of τ_E and of power at the device (d) Ramsey dephasing measurement. Points: fringe amplitude as a function of τ_S. Curve: Gaussian fit. Left inset: Ramsey pulse cycle. Right inset: signal as a function of phase difference, with $\tau_S = 5$ ns. (e) Hahn echo measurement. Points: fringe amplitude. Line: fit (see text). Right inset: fringes for orthogonal phases of the echo pulse (along x and y axes in the qubit's rotating frame), with $\tau_S = 10$ ns. In panels (c)–(e), $\theta = 15°$, $B = 83$ mT, and $f = 2.82$ GHz.

effective parallel g factor $g = 2.22 \pm 0.02$, which is nearly eight times smaller than the right dot g_{orb} extracted above from transport measurements but consistent with transport spectroscopy of the left dot [17].

Qubit dephasing is measured using pulsed spectroscopy [11,37]. We operate at $|\mathbf{B}| = 83$ mT, $\theta = 15°$, and $f_R = 2.82$ GHz, which gives good contrast of the pulsed ΔI. (Previous experiments [11] found dephasing independent of $|\mathbf{B}|$ and θ.) Applying a single microwave burst of duration τ_E per pulse cycle drives coherent Rabi oscillations between qubit states [Fig. 4(c)]. As expected, Rabi frequency increases with microwave power but saturates at the highest power, suggesting a contribution of short-range disorder to the EDSR mechanism [40]. With coherent manipulation established, we measure dephasing using a Ramsey sequence of two bursts per pulse cycle separated by time τ_S [Fig. 4(d)]. As a function of phase difference ϕ between bursts, ΔI shows fringes whose amplitude decays

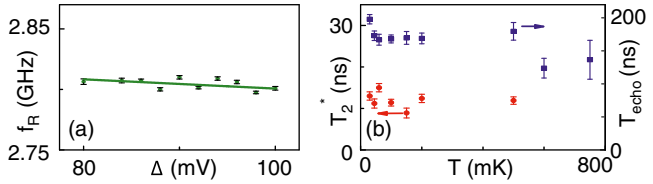

FIG. 5. (a) Qubit frequency as a function of pulse amplitude (points) with linear fit. (b) Measured T_2^* (circles) and T_{echo} (squares) as a function of temperature. Above 750 mK, incoherent current leakage prevents EDSR measurement.

as $e^{-(\tau_S/T_2^*)^2}$, where T_2^* is the dephasing time. A fit to the data gives $T_2^* = 13 \pm 1$ ns. Using a Hahn echo sequence [Fig. 4(e)] to cancel out slowly varying noise, the amplitude decays more slowly and is phenomenologically fit by $e^{-(\tau_S/T_{\mathrm{echo}})^\gamma}$, with fitted coherence time $T_{\mathrm{echo}} = 198 \pm 7$ ns and $\gamma = 1.7 \pm 0.2$.

These values are similar to previous measurements on a spin-valley qubit [11]. That experiment did not allow conclusive determination of dephasing or decoherence mechanisms, with charge noise [16] and hyperfine coupling [1,10] being leading candidates. In our device, we now show that charge noise does not limit T_2^*. By changing the pulse voltage Δ for the manipulation step [Fig. 4(a)], we measure the dependence of f_R on gate voltage [Fig. 5(a)]. A linear fit gives $df_R/d\Delta = -0.4 \pm 0.3$ MHz/mV. (The orthogonal axis in gate space showed a similarly weak dependence [17].) Thus, to explain the measured T_2^* by noise on the detuning axis would require root-mean-square voltage noise $\Delta_{\mathrm{rms}} \geq 27$ mV [41]. Since this is broader than the narrowest transport features, this mechanism can be ruled out [17]. By a similar argument, the noise level to account for the measured T_{echo} would be $\Delta_{\mathrm{rms}} \gtrsim 2$ mV [41]. This is consistent with the data, although greater than the estimated instrument noise, implying an origin in the device itself. It is also approximately consistent (roughly six times larger) with an independent measurement of charge noise in a similar device [16]. Temperature dependence of T_2^* and T_{echo} is shown Fig. 5(b).

In conclusion, both leakage current and qubit dephasing imply hyperfine coupling to a randomly fluctuating spin bath of ^{13}C nuclei in each quantum dot, with effective coupling strength $E_N \sim 0.16$ μeV. Considering the estimated 6×10^4 nuclei in each dot and 1.1% ^{13}C abundance, this implies hyperfine constant $\mathcal{A} \sim 4 \times 10^{-4}$ eV. This is consistent with other measurements on isotopically purified [10] and natural [11] nanotube devices but continues a long-standing discrepancy with numerical simulations [36,42,43] and bulk spectroscopy of fullerenes [44] and nanotubes [45,46]. Hyperfine interaction may also limit T_{echo}, but since the measured value implies unexpectedly rapid nuclear spin diffusion [17], we suspect that charge noise is more significant. This would indicate the spin-valley qubit is sensitive to electric fields, for example, because of interdot exchange [11,47].

We acknowledge Templeton World Charity Foundation, EPSRC (EP/J015067/1), Marie Curie CIG and IEF fellowships, Stiftung der Deutschen Wirtschaft, and the Royal Academy of Engineering.

*tian.pei@materials.ox.ac.uk
†edward.laird@materials.ox.ac.uk

[1] H. O. H. Churchill, A. J. Bestwick, J. W. Harlow, F. Kuemmeth, D. Marcos, C. H. Stwertka, S. K. Watson, and C. M. Marcus, Nat. Phys. **5**, 321 (2009).
[2] K. Flensberg and C. M. Marcus, Phys. Rev. B **81**, 195418 (2010).
[3] F. Pei, E. A. Laird, G. A. Steele, and L. P. Kouwenhoven, Nat. Nanotechnol. **7**, 630 (2012).
[4] J. J. Viennot, M. C. Dartiailh, A. Cottet, and T. Kontos, Science **349**, 408 (2015).
[5] C. Ohm, C. Stampfer, J. Splettstoesser, and M. Wegewijs, Appl. Phys. Lett. **100**, 143103 (2012).
[6] A. Pályi, P. R. Struck, M. S. Rudner, K. Flensberg, and G. Burkard, Phys. Rev. Lett. **108**, 206811 (2012).
[7] B. Braunecker, P. Burset, and A. Levy Yeyati, Phys. Rev. Lett. **111**, 136806 (2013).
[8] M. C. Hels, B. Braunecker, K. Grove-Rasmussen, and J. Nygård, Phys. Rev. Lett. **117**, 276802 (2016).
[9] F. Kuemmeth, S. Ilani, D. C. Ralph, and P. L. McEuen, Nature (London) **452**, 448 (2008).
[10] H. O. H. Churchill, F. Kuemmeth, J. W. Harlow, A. J. Bestwick, E. I. Rashba, K. Flensberg, C. H. Stwertka, T. Taychatanapat, S. K. Watson, and C. M. Marcus, Phys. Rev. Lett. **102**, 166802 (2009).
[11] E. A. Laird, F. Pei, and L. P. Kouwenhoven, Nat. Nanotechnol. **8**, 565 (2013).
[12] E. A. Laird, F. Kuemmeth, G. A. Steele, K. Grove-Rasmussen, J. Nygård, K. Flensberg, and L. P. Kouwenhoven, Rev. Mod. Phys. **87**, 703 (2015).
[13] F. H. L. Koppens, J. A. Folk, J. M. Elzerman, R. Hanson, L. H. W. van Beveren, I. T. Vink, H. P. Tranitz, W. Wegscheider, L. P. Kouwenhoven, and L. M. K. Vandersypen, Science **309**, 1346 (2005).
[14] S. Nadj-Perge, S. M. Frolov, J. W. W. van Tilburg, J. Danon, Y. V. Nazarov, R. Algra, E. P. A. M. Bakkers, and L. P. Kouwenhoven, Phys. Rev. B **81**, 201305 (2010).
[15] C. C. Wu, C. H. Liu, and Z. Zhong, Nano Lett. **10**, 1032 (2010).
[16] A. Mavalankar, T. Pei, E. M. Gauger, J. H. Warner, G. A. D. Briggs, and E. A. Laird, Phys. Rev. B **93**, 235428 (2016).
[17] See Supplemental Materials at http://link.aps.org/supplemental/10.1103/PhysRevLett.118.177701 for fabrication, Coulomb spectroscopy, modeling, and dephasing mechanisms, including Ref. [47].
[18] O. N. Jouravlev and Y. V. Nazarov, Phys. Rev. Lett. **96**, 176804 (2006).
[19] R. Winkler, S. Papadakis, E. De Poortere, and M. Shayegan, *Spin—Orbit Coupling Effects in Two-Dimensional Electron and Hole Systems* (Springer, 2003), Vol. 41.
[20] W. G. van der Wiel, S. De Franceschi, J. M. Elzerman, T. Fujisawa, S. Tarucha, and L. P. Kouwenhoven, Rev. Mod. Phys. **75**, 1 (2002).
[21] G. A. Steele, G. Gotz, and L. P. Kouwenhoven, Nat. Nanotechnol. **4**, 363 (2009).
[22] K. Ono, D. G. Austing, Y. Tokura, and S. Tarucha, Science **297**, 1313 (2002).
[23] E. Minot, Y. Yaish, V. Sazonova, and P. L. McEuen, Nature (London) **428**, 536 (2004).
[24] G. A. Steele, F. Pei, E. A. Laird, J. M. Jol, H. B. Meerwaldt, and L. P. Kouwenhoven, Nat. Commun. **4**, 1573 (2013).
[25] T. S. Jespersen, K. Grove-Rasmussen, J. Paaske, K. Muraki, T. Fujisawa, J. Nygård, and K. Flensberg, Nat. Phys. **7**, 348 (2011).
[26] G. Széchenyi and A. Pályi, Phys. Rev. B **88**, 235414 (2013).
[27] G. Széchenyi and A. Pályi, Phys. Rev. B **91**, 045431 (2015).
[28] M. D. Schroer, K. D. Petersson, M. Jung, and J. R. Petta, Phys. Rev. Lett. **107**, 176811 (2011).
[29] M. Brauns, J. Ridderbos, A. Li, E. P. A. M. Bakkers, W. G. van der Wiel, and F. A. Zwanenburg, Phys. Rev. B **94**, 041411 (2016).
[30] R. Li, F. E. Hudson, A. S. Dzurak, and A. R. Hamilton, Nano Lett. **15**, 7314 (2015).
[31] S. Nadj-Perge, V. S. Pribiag, J. W. G. van den Berg, K. Zuo, S. R. Plissard, E. P. A. M. Bakkers, S. M. Frolov, and L. P. Kouwenhoven, Phys. Rev. Lett. **108**, 166801 (2012).
[32] A. Pfund, I. Shorubalko, K. Ensslin, and R. Leturcq, Phys. Rev. Lett. **99**, 036801 (2007).
[33] J. Danon and Y. V. Nazarov, Phys. Rev. B **80**, 041301 (2009).
[34] J. Klinovaja, M. J. Schmidt, B. Braunecker, and D. Loss, Phys. Rev. B **84**, 085452 (2011).
[35] A. Pályi and G. Burkard, Phys. Rev. B **80**, 201404(R) (2009).
[36] G. Csiszár and A. Pályi, Phys. Rev. B **90**, 245413 (2014).
[37] F. H. L. Koppens, C. Buizert, K.-J. Tielrooij, I. T. Vink, K. C. Nowack, T. Meunier, L. P. Kouwenhoven, and L. M. K. Vandersypen, Nature (London) **442**, 766 (2006).
[38] E. A. Laird, C. Barthel, E. I. Rashba, C. M. Marcus, M. P. Hanson, and A. C. Gossard, Phys. Rev. Lett. **99**, 246601 (2007).
[39] K. C. Nowack, F. H. L. Koppens, Y. V. Nazarov, and L. M. K. Vandersypen, Science **318**, 1430 (2007).
[40] G. Széchenyi and A. Pályi, Phys. Rev. B **89**, 115409 (2014).
[41] J. M. Taylor, J. R. Petta, A. C. Johnson, A. Yacoby, C. M. Marcus, and M. D. Lukin, Phys. Rev. B **76**, 035317 (2007).
[42] O. Yazyev, Nano Lett. **8**, 1011 (2008).
[43] J. E. Fischer, B. Trauzettel, and D. Loss, Phys. Rev. B **80**, 155401 (2009).
[44] C. H. Pennington and V. A. Stenger, Rev. Mod. Phys. **68**, 855 (1996).
[45] Y. Ihara, P. Wzietek, H. Alloul, M. Rummeli, T. Pichler, F. Simon, and M. H. Rümmeli, Europhys. Lett. **90**, 17004 (2010).
[46] A. Kiss, A. Pályi, Y. Ihara, P. Wzietek, P. Simon, H. Alloul, V. Zólyomi, J. Koltai, J. Kürti, B. Dóra *et al.*, Phys. Rev. Lett. **107**, 187204 (2011).
[47] Y. Li, S. C. Benjamin, G. A. D. Briggs, and E. A. Laird, Phys. Rev. B **90**, 195440 (2014).